CrystEngComm

PAPER

View Article Online
View Journal | View Issue

Check for updates

Cite this: *CrystEngComm*, 2025, **27**, 7379

Quadrupolar NMR crystallography guided crystal structure prediction (QNMRX-CSP) of zwitterionic organic HCl salts

Carl H. Fleischer III,[ab] Sean T. Holmes[ab] and Robert W. Schurko*[ab]

Received 16th September 2025,
Accepted 21st October 2025

DOI: 10.1039/d5ce00899a

rsc.li/crystengcomm

In this work, we benchmark quadrupolar NMR crystallography guided crystal structure prediction (QNMRX-CSP) for determining the crystal structures of two zwitterionic organic HCl salts, L-ornithine HCl (**Orn**) and L-histidine HCl·H_2O (**Hist**). These salts present an interesting challenge for QNMRX-CSP, as gas-phase geometry optimizations used to generate starting structures for the organic zwitterionic fragments fail to capture their correct solid-state geometries. To overcome this limitation, geometry optimizations using the COSMO water-solvation model are employed to generate initial structural models. Using this approach, QNMRX-CSP yields structural models of the two zwitterionic organic HCl salts that closely match experimentally determined crystal structures. In addition, the application of QNMRX-CSP to **Hist** represents a further step toward the *de novo* structural determination of solvated organic HCl salts, as **Hist** is the first benchmark system of this type to include a water molecule as a component of its crystal structure. This work is significant for its potential application to the structural determination of active pharmaceutical ingredients, which often feature complex organic components and solvated solid forms.

1. Introduction

NMR crystallography (NMRX) is a powerful approach for determining and refining the structures of crystalline solids, particularly when conventional methods face limitations. NMRX integrates solid-state NMR (SSNMR) spectroscopy, X-ray diffraction (most often powder X-ray diffraction, PXRD), and quantum chemical calculations to provide a comprehensive picture of atomic-level structure.[1–5] SSNMR offers detailed information about local atomic environments, interatomic distances, and molecular conformations;[6] XRD reveals long-range order, symmetry, space groups, and unit cell parameters;[7,8] and quantum chemical calculations can be used to generate and refine candidate structures,[9–16] as well as to calculate NMR interaction tensors, which can be used for screening and validation.[17–19] Collectively, these enable the *de novo* structural determination of complex solids, including those with multiple components (*i.e.*, organic molecules, inorganic ions, solvate molecules, *etc.*),[20,21] structures with poorly defined hydrogen atom positions,[22,23] and even disordered materials.[24,25] Since the bonding and spatial arrangements of atoms directly relate to physicochemical properties such as solubility, stability, and bioavailability, NMRX provides a means of probing structure–property–function relationships in a wide range of organic solids, including active pharmaceutical ingredients and numerous other functional materials.[1–5]

In NMRX methods, the choice of the most diagnostically relevant NMR interaction (*e.g.*, chemical shifts,[1,26–29] dipolar couplings,[30–34] or the quadrupolar interaction[35–41]) is strongly sample-dependent. To date, most NMRX studies have employed isotropic chemical shifts due to their ease of measurement and wide availability;[1–5] however, there are key limitations. First, calculating chemical shifts with first-principles quantum chemical computations can be computationally expensive, especially for structures featuring many atoms and/or for large datasets of candidate structures (we note that there are emerging machine-learning methods, such as the ShiftML software packages, that enable rapid computation of chemical shifts).[19,42,43] Second, in certain cases, chemical shift assignment is fraught with difficulties due to broad patterns resulting from homo- and heteronuclear dipolar couplings[44–47] and/or peak overlap due to the sample featuring multiple similar chemical environments – this is particularly problematic for complex molecules in organic solids, especially those with multiple low energy conformations.[1]

The quadrupolar interaction, which provides an alternative to chemical shifts for NMRX studies, manifests only in the SSNMR spectra of quadrupolar nuclides (*i.e.*, nuclear spins $I > \frac{1}{2}$). The quadrupolar interaction arises from

---

[a] *Department of Chemistry & Biochemistry, Florida State University, Tallahassee, FL 32306, USA. E-mail: rschurko@fsu.edu*

[b] *National High Magnetic Field Laboratory, Florida State University, Tallahassee, FL, 32310, USA*

the coupling between the nuclear quadrupole moment (Q) and the electric field gradients (EFGs) at the nucleus. EFGs are described by traceless, symmetric, second-rank tensors, which are defined by three principal components in their own principal axis systems, ranked such that $|V_{33}| \geq |V_{22}| \geq |V_{11}|$. The EFG tensor components are most often expressed in terms of two parameters: the quadrupolar coupling constant, $C_Q = eQV_{33}/h$, and the quadrupolar asymmetry parameter, $\eta_Q = (V_{11} - V_{22})/V_{33}$, where e is the elementary charge, h is Planck's constant, and $0 \leq \eta_Q \leq 1$. Since EFGs depend solely on the ground state electron density, they are calculated from first principles more efficiently than chemical shifts.[48,49]

In light of this, as well as the abundance of quadrupolar nuclides in many solid organic compounds, our group developed a protocol for elucidating the solid-state structures of organic HCl salts, termed quadrupolar NMR crystallography guided crystal structure prediction (QNMRX-CSP).[40,41] QNMRX-CSP employs powder X-ray diffraction (PXRD), ^{35}Cl EFG tensors (both experimentally measured and calculated with DFT), Monte-Carlo simulated annealing (MC-SA),[9] and dispersion-corrected density functional theory (DFT-D2*) geometry optimizations.[50] To date, three studies have reported the development and application of QNMRX-CSP: (i) the initial study described the development of the protocol and its application to seven organic HCl salts, including five used as benchmarking systems, and two used in blind prediction tests;[40] (ii) the second study extended the benchmarking of QNMRX-CSP to two organic HCl salts featuring organic components larger than those in the first set, and explored the application of QNMRX-CSP in the absence of PXRD data;[41] and (iii) the most recent study demonstrated the application of QNMRX-CSP for the first *de novo* structure determination of an organic HCl salt for which no prior crystal structure was known.[51] The studies highlight the necessity for continued benchmarking and the investigation of a more diverse range of organic HCl salts.

Herein, we extend QNMRX-CSP benchmarking calculations to zwitterionic organic HCl salts, including L-ornithine HCl (**Orn**) and L-histidine HCl·H_2O (**Hist**) (Scheme 1). This study focuses on zwitterionic organic HCl salts, since they offer opportunities to tune the physiochemical properties of solid forms, while also presenting several challenges for the application of QNMRX-CSP. To this end, benchmarking calculations were carried out in two distinct scenarios: (i) to assess whether QNMRX-CSP can identify valid structural candidates for zwitterionic organic HCl salts using a known crystal structure as a starting point, and (ii) to evaluate its ability to generate accurate structural models using only the molecular formula, space group, and unit cell parameters. In the second scenario, geometry optimizations were performed using the COSMO water-solvation model to generate reasonable starting structural models. These two scenarios were explored independently: the first serves as a benchmarking exercise, while the second simulates a "real-world" application of QNMRX-CSP. **Orn** and **Hist** were chosen as structural models since they have known crystal structures and precisely measured ^{35}Cl EFG tensors.[52–57] Moreover, a water molecule is present in the crystal structure of **Hist**, which makes structural determination more difficult, but also opens the possibility of the *de novo* structure determination of solvated organic HCl salts by QNMRX-CSP.

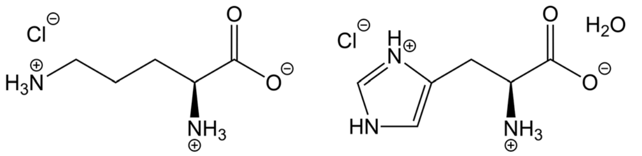

Scheme 1 Molecular diagrams of the zwitterionic forms of L-ornithine HCl (**Orn**, left) and L-histidine HCl·H_2O (**Hist**, right).

2. Methods

2.1 QNMRX-CSP

QNMRX-CSP was developed and benchmarked for determining the crystal structures of organic HCl salts (Scheme S1 depicts a schematic diagram of QNMRX-CSP).[40,41] QNMRX-CSP has three modules, each of which is divided into several steps: (i) module 1 (M1) involves the development of "chemically sensible" molecular fragments; (ii) module 2 (M2) uses the polymorph software to generate the initial candidate structures with MC-SA; and (iii) module 3 (M3) uses a QNMRX routine featuring DFT-D2* calculations to obtain geometry-optimized structural models and their concomitant ^{35}Cl EFG tensors. In M2 and M3, benchmarked metrics are applied to retain candidate structures likely to converge to the "correct" crystal structure (§2.3). Lastly, the best candidate structures are validated using structural validation terms (§2.4).

2.2 Computational details

QNMRX-CSP uses several software packages, including Amsterdam density functional (ADF),[58] Polymorph[9] and CASTEP[59] within the BIOVIA Materials Studio R3 suite, and CASTEP Data Manager, an in-house program that automates CASTEP calculations.[40]

Amsterdam density functional. Geometry optimizations of the organic zwitterions **Orn** and **Hist** were performed using ADF to generate molecular fragments for subsequent use in polymorph. Molecular fragments are defined as chemically meaningful, rigid molecules that are treated as a single unit during structure generation where the relative atomic positions are held constant (*i.e.*, motion groups) and have a set of Hirshfeld charges applied to each atom (Table S1) – herein, this specifically refers to the organic zwitterionic cation, Cl$^-$ ion, and water molecule (see §3.1 for further discussion). Geometry optimizations employed the COSMO water-solvation model[60,61] using the Allinger radii,[62] RPBE functional,[63] TZ2P basis set,[64] and frozen core approximation.[65] The convergence quality of the geometry optimizations was set to normal, corresponding to an energy change of 10^{-5} Ha, in gradients of 10^{-3} Ha Å^{-1}, and a maximum step of 0.01 Å.

Polymorph. Polymorph used the aforementioned molecular fragments of **Orn** and **Hist**, along with their space groups, to generate candidate structures. Polymorph employs a four-step routine to generate a maximum of 10 000 candidate crystal structures per trial, where one trial consists of one complete iteration of (i) packing, (ii) clustering, (iii) force-field geometry optimization, and (iv) clustering (second round). The packing step uses a MC-SA algorithm to generate candidate crystal structures with maximum and minimum temperatures of 1.5×10^5 K and 300 K, respectively, using heating and cooling factors of 0.025 and 0.0005, and a minimum move factor of 10^{-10}. Clustering removes duplicate structures using a radial distribution cut-off of 7.0 Å, tolerance of 0.13, and 140 bins. Dreiding force-field[66] geometry optimizations were used to refine the candidate structures (the relative atomic positions for atom(s) in a molecular fragment are held constant) and calculate their static lattice energies. Convergence for these geometry optimizations is reached after maximum changes are achieved in energy of 2×10^{-5} kcal mol^{-1}, force of 10^{-3} kcal mol^{-1} Å^{-1}, stress of 10^{-3} GPa, and atomic displacement of 10^{-5} Å. Duplicate structures were removed in the second clustering step, using the same thresholds as the first. After ten trials of polymorph, a third round of clustering removed duplicate candidate structures generated across all trials.

CASTEP. Plane-wave DFT-D2*[43] geometry optimizations and subsequent calculations of NMR interaction tensors were conducted in CASTEP. Two DFT-D2* geometry optimization approaches were used: (i) truncated and (ii) convergent. These approaches differ in how they implemented the L-BFGS scheme:[67] a truncated geometry optimization sets the number of BFGS cycles to 5, whereas a convergent geometry optimization allows for progression to full convergence. Both approaches use the RPBE functional,[63] ultrasoft pseudopotentials generated on-the-fly,[68] the zeroth-order regular approximation,[69] a planewave energy cut-off value of 800 eV, and a *k*-point spacing of 0.05 Å^{-1} using the Monkhorst–Pack grid.[70] Convergence thresholds are a maximum change in energy of 5×10^{-6} eV per atom, displacement of 5×10^{-4} Å, and force of 10^{-2} eV Å^{-1}. Calculated ^{35}Cl EFG tensor principal components were converted to the MHz scale using a nuclear quadrupole moment of $Q(^{35}\mathrm{Cl}) = -8.17$ fm^2.[71]

2.3 Metrics

QNMRX-CSP uses metrics to retain candidate structures that are most likely to converge to the "correct" structure. Metrics include the experimental unit cell parameters, calculated static lattice energies, and ^{35}Cl EFG tensors. The thresholds for these metrics were previously determined in benchmarking studies and further validated by two blind tests,[40,41] as well as a *de novo* structure determination.[51] Herein, four metric sets are used, which are combinations of metrics that are strategically positioned throughout the modules of QNMRX-CSP (see §3.1, Table 1, and Scheme S1). Candidate structures are only retained if both thresholds in each metric set are satisfied.

Unit cell parameters. The unit cell parameters of the candidate structures were compared to those of the known crystal structures of **Orn** and **Hist** (Table 2; ORNHCL12[52] and HISTCM12,[53] respectively). Candidates were retained if their predicted unit cell parameters were within ±20% for **Orn** and ±10% for **Hist** of the known values.

Static lattice energies. The static lattice energy metrics were employed differently in M2 and M3. At the end of M2, the calculated static lattice energy of each candidate structure, E_{lat}, was compared to the candidate structure in the set with the lowest calculated static lattice energy, E_{low}. Candidate structures having E_{lat} values in the bottom 13.5% of the set were retained, such that:

$$E_{\mathrm{low}} \leq E_{\mathrm{lat}} \leq 0.865 \cdot E_{\mathrm{low}} \tag{1}$$

In M3, candidate structures were retained after each round of geometry optimizations, provided that E_{lat} values were less than or equal to a benchmarked threshold energy (E_{thresh}), such that:

$$\Delta E_{\mathrm{lat}} = E_{\mathrm{lat}} - E_{\mathrm{low}} \leq E_{\mathrm{thresh}} \tag{2}$$

The value of E_{thresh} changes depending on its position in M3 as part of metric set 2, metric set 3, and metric set 4 with values of 135 kJ mol^{-1}, 50 kJ mol^{-1}, and 1 kJ mol^{-1}, respectively (Scheme S1).

Table 1 QNMRX-CSP metric sets and the benchmarked metric thresholds

Metric set	Unit cell parameters[a]	E_{lat}[b]	Γ_{EFG}[c] (MHz)	E_{thresh}[d] (kJ mol^{-1})
1	±20%/±10%	13.5%	—	—
2	—	—	0.70	135
3	—	—	0.49	50
4	—	—	0.49	1

[a] The unit cell parameters of the candidate structures are compared to the known unit cell parameters (Table 2) and are retained if those values are within ±20% or ±10% for **Orn** and **Hist**, respectively. [b] Candidate structures in the bottom 13.5% of E_{lat} values are retained, *i.e.*, such that: $E_{\mathrm{low}} \leq E_{\mathrm{lat}} \leq 0.865 \cdot E_{\mathrm{low}}$, where E_{low} is the E_{lat} of lowest of all candidate structures. [c] Candidate structures are retained if their Γ_{EFG} is equal to or below the benchmarked threshold. [d] Candidate structures are retained if their E_{lat} is equal to or below E_{thresh}, such that: $\Delta E = E_{\mathrm{lat}} - E_{\mathrm{low}} \leq E_{\mathrm{thresh}}$.

Table 2 Crystallographic information and ^{35}Cl EFG tensors of **Orn** and **Hist**[a,b]

	Space group	a (Å)	b (Å)	c (Å)	α (°)	β (°)	γ (°)	C_Q (MHz)	η_Q
Orn	$P2_1$	9.9480	7.9637	4.9826	90	99.87	90	2.99	0.36
Hist	$P2_12_12_1$	15.36	8.92	6.88	90	90	90	1.81	0.64

[a] The crystallographic information of **Orn** and **Hist** was obtained from their known crystal structures, ORNHCL12[52] and HISTCM12,[53] respectively. [b] The experimental ^{35}Cl EFG tensor parameters of **Orn** and **Hist** were obtained from previous studies.[54–57] The quadrupolar coupling constant and asymmetry parameter are given by $C_Q = eQV_{33}/h$, and $\eta_Q = (V_{11} - V_{22})/V_{33}$, respectively. The principal components of the EFG tensors are defined such that $|V_{33}| \geq |V_{22}| \geq |V_{11}|$. The sign of C_Q cannot be determined from the experimental spectra.

^{35}Cl EFG distance. The ^{35}Cl EFG distance (Γ_{EFG}) was employed to assess the similarity between the calculated and experimental ^{35}Cl EFG tensors:[72]

$$\Gamma_{\text{EFG}} = \left(\frac{1}{15}\left[3\Delta_{11}^{\ 2} + 3\Delta_{22}^{\ 2} + \ 3\Delta_{33}^{\ 2} + 2\Delta_{11}\Delta_{22} + 2\Delta_{22}\Delta_{33} + 2\Delta_{11}\Delta_{33}\right]\right)^{1/2} \tag{3}$$

$$\Delta_{kk} = \left|V_{kk}^{\text{calc}} - V_{kk}^{\text{exp}}\right| \tag{4}$$

where V_{kk} (k = 1, 2, 3) are the principal components of the ^{35}Cl EFG tensors and $|V_{11} \leq |V_{22}| \leq |V_{33}|$. An Γ_{EFG} value of zero indicates that the two ^{35}Cl EFG tensors are identical.

2.4 Structural validation

QNMRX-CSP validates candidate structures using two terms: the *R*-factor (*R*), which compares PXRD patterns, and an atomic position RMSD parameter, Δ_{RMSD}, which compares atomic positions of the candidate structures to those of geometry-optimized structural models derived from experimental crystal structures. The CSD has over 1.3 million structures, of which *ca.* 90% have an $R \leq 10\%$; accordingly, we considered an $R \leq 10\%$ to indicate a reasonable structural match.[73] In the most recent CCDC blind tests, structures were considered a match if their $\Delta_{\text{RMSD}} \leq 1$ Å.[74,75] This relatively large threshold reflects the criteria used in these blind tests, which account for molecular size and flexibility, as well as the unique unit cell parameters of each structure. Herein, we adopted a stricter definition of a structural match, since the known unit cell parameters were used in the calculations. This resulted in smaller Δ_{RMSD} values, with structures exhibiting $\Delta_{\text{RMSD}} \leq 0.2$ Å considered to be good matches.

***R*-Factors.** PXRD patterns were simulated using the Powder Pattern tool in Mercury 2022.3.0 with a Cu Kα radiation source (λ = 1.54056 nm), 2θ ranging from 5° to 50°, a step size of 0.01°, and a full-width half height peak width of 0.05°. The comparison of PXRD patterns employs the *R*-factor:

$$R = \frac{\sum\left|\left(|F_0| - |F_c|\right)\right|}{\sum|F_0|} \times 100\% \tag{5}$$

where F_0 and F_c are the calculated structure factor amplitudes of the reference and candidate structures, respectively, and the sum is over all reflections used in the refinement.

Atomic position RMSDs. Δ_{RMSD} values were calculated using the CSD-Materials Crystal Packing Similarity module in Mercury 2022.3.0 using a 15-molecule cluster, using distance and angle tolerances of 20% and 20°, respectively.

3. Results and discussion

3.1 QNMRX-CSP

To further develop QNMRX-CSP and expand its applicability to a wider array of systems, it is essential to refine benchmarking protocols, validate the thresholds used in its metric sets, and evaluate its performance for systems featuring a diverse selection of molecular fragments (*e.g.*, organic zwitterions) and multiple motion groups (*e.g.*, hydrates). Accordingly, QNMRX-CSP was applied in two different scenarios: first, to ascertain whether QNMRX-CSP can determine valid structural candidates using a fragment from the known crystal structure as a starting point, the steps outlined in module 1A (M1(A)) were followed (§3.2). Second, to demonstrate that valid structural candidates can be determined with knowledge of only the molecular formula, space group, and unit cell parameters (§3.3), the steps in module 1B (M1(B)) were used. Both scenarios subsequently used M2 and M3 in an identical manner. These two scenarios were investigated independently, with the first serving as a benchmarking and validation exercise, and the second as a practical application of QNMRX-CSP.

Module 1A. Application of M1(A) consists of four steps: (i) the known crystal structures (ORNHCL12 (ref. 52) and HISTCM12 (ref. 53)) were obtained from the Cambridge Structural Database; (ii) these crystal structures were geometry optimized using convergent DFT-D2* calculations in CASTEP; (iii) the resulting structural models were unbuilt (*i.e.*, asymmetric units were extracted) and the calculated Hirshfeld charges from the geometry optimization were applied; and (iv) the organic zwitterion, Cl$^-$ ion, and water molecule (applicable only for **Hist**) were assigned as independent motion groups.

Module 1B. Application of M1(B) also consists of four steps: (i) the organic zwitterions were built in Materials Studio, based only upon the molecular formula (Scheme 1); (ii) either: (a) the organic zwitterion was centered in a 15 × 15 × 15 Å^3 unit cell with a space group of $P1$ and subjected to a convergent geometry optimization, or (b) a geometry

Table 3 The number of candidate structures for each starting point for the QNMRX-CSP protocol for **Orn** and **Hist**

	Known crystal structures[a]			Refined isolated molecule[b]		
Orn	Initial		Retained	Initial		Retained
Metric set 1[c]	30 733	→	71	52 017	→	749
Metric set 2	71	→	18	749	→	133
Metric set 3	18	→	6	133	→	16
Metric set 4	6	→	1	16	→	3
Hist						
Metric set 1	64 952	→	166	63 542	→	179
Metric set 2	166	→	5	179	→	4
Metric set 3	5	→	3	4	→	2
Metric set 4	3	→	2	2	→	2

[a] The starting point for these calculations was geometry-optimized structures based on a known crystal structure. [b] The starting point for these calculations was ADF geometry-optimized structures based on isolated molecules. [c] The metric sets and their corresponding benchmarked metric values are detailed in Table 1.

optimization was performed in ADF with implicit solvent embedding *via* the COSMO model; (iii) the Cl^- ion and water molecule (the latter applicable only for **Hist**) were added and the tabulated Hirshfeld charges were applied (Table S1); and (iv) the organic zwitterion, Cl^- ion, and water molecule were assigned as independent motion groups.

Module 2. M2 employs polymorph in a four-step routine (§2.2) for 10 trials for both **Orn** and **Hist**. Metric set 1 was then applied (Table 1; §2.3), which retains candidate structures by comparing their respective unit cell parameters to those of the known crystal structures, as well as the relative E_{lat} values among the candidate structures.

Module 3. M3 involves: (i) truncated geometry optimizations (§2.2) and subsequent ^{35}Cl EFG tensor calculations on the candidate structures, followed by the application of metric set 2; (ii) convergent geometry optimizations and subsequent calculation of the ^{35}Cl EFG tensors for the candidate structures, followed by the application of metric set 3; and (iii) adjustment of the unit cell parameters of the candidate structures to those of the experimental unit cell parameters, followed by a convergent geometry optimization, calculation of ^{35}Cl EFG tensors, and the application of metric set 4. The experimental ^{35}Cl EFG tensors used for comparison were obtained from previous studies (Table 2).[54–57]

Structural validation. Finally, the remaining candidate structures were validated (§2.4) by calculating their R (for comparison of simulated PXRD patterns) and Δ_{RMSD} values (for direct comparison to DFT-D2* geometry optimized known crystal structures).

3.2 QNMRX-CSP of zwitterionic organic HCl salts: starting from the known crystal structures

To demonstrate that QNMRX-CSP can be applied to organic zwitterionic HCl salts, we performed benchmarking calculations on **Orn** and **Hist**. A summary of the number of candidate structures retained by each metric set is provided in Table 3.

QNMRX-CSP, following M1(A), was first applied to **Orn**, which involved assigning molecular fragments consisting of an organic zwitterion and Cl^- ion. Polymorph was then applied to generate 30 733 candidate structures. Of these, 71 were retained following the application of metric set 1. In M3, the 71 candidate structures underwent truncated geometry optimizations, followed by the application of metric set 2, which retained 18 candidate structures. These 18 candidate structures then underwent convergent geometry optimizations followed by the application of metric set 3, which retained 6 structures. These structures had their unit cell parameters adjusted to match those of the known crystal structure (Table 2) and were refined with a convergent geometry optimization. Of these, only 1 structure was retained by metric set 4, which is denoted as structure 6-11 (Fig. 1A). For structural validation (Table 4), the simulated PXRD pattern of 6-11 was compared to that of the DFT-D2*

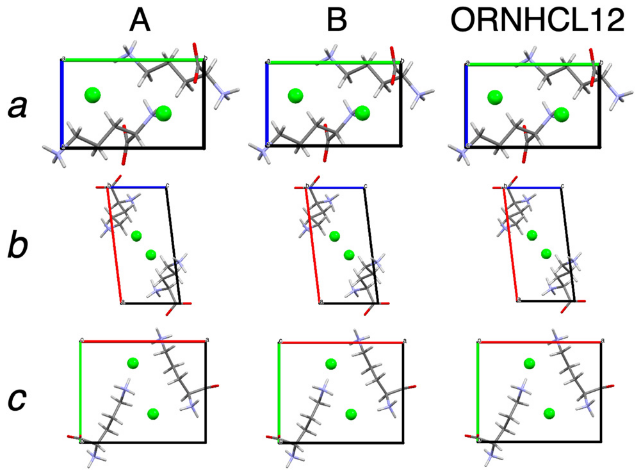

Fig. 1 Projections of the unit cells along the *a*, *b*, and *c* crystallographic axes for the crystal structure of **Orn** determined by QNMRX-CSP starting from the known crystal structure (A; §3.2) and an isolated molecule (B; §3.3), and the geometry-optimized crystal structure of **Orn** (ORNHCL12).

Table 4 Calculated ^{35}Cl EFG tensors and structural validation terms for each validated candidate structure from QNMRX-CSP

Orn or **Hist**	Structure	$C_Q{}^a$ (MHz)	$\eta_Q{}^a$	$\Gamma_{EFG}{}^b$ (MHz)	R^c (%)	$\Delta_{RMSD}{}^c$ (Å)
Starting from the known crystal structures[d]						
Orn	6-11	3.009	0.41	0.043	2.09	0.003
Hist	6-617	1.814	0.60	0.018	6.67	0.070
Hist	2-452	1.819	0.56	0.037	6.72	0.070
Starting from refined isolated molecules[e]						
Orn	9-625	3.026	0.41	0.049	2.39	0.003
Orn	8-302	3.025	0.41	0.049	2.41	0.003
Orn	7-408	3.012	0.40	0.036	2.45	0.003
Hist	8-331	1.753	0.78	0.067	5.15	0.050
Hist	7-392	1.738	0.80	0.078	6.47	0.058

[a] The calculated ^{35}Cl EFG tensors for the candidate structures. [b] The Γ_{EFG} of the candidate structures was derived using their calculated ^{35}Cl EFG tensors and those reported from experiments (Table 2). [c] The R and Δ_{RMSD} values were derived using the crystal structures determined from QNMRX-CSP and the methods outlined in §2.4. [d] The candidate structures were obtained from geometry-optimized structures based on the known crystal structures. [e] The candidate structures were obtained from ADF geometry-optimized structures based on isolated molecules.

geometry-optimized ORNHCL12 structure, yielding an R value of 2.09%, well below the 10% threshold. Furthermore, a comparison of the atomic positions between the two structures yields Δ_{RMSD} = 0.003 Å, well below the 0.2 Å threshold. Hence, 6-11 is an excellent structural match with the refined structure **Orn** (Fig. 1).

Application of QNMRX-CSP to **Hist** follows a similar routine; however, the resolution of final candidate structures was more challenging due to the presence of a water molecule as a third motion group. This is reflected by the higher number of unique candidate structures predicted in M2 with the Polymorph routine (64 952 structural candidates as opposed to 30 733 for **Orn**). Because of the larger phase space sampled by MC-SA due to the presence of a water molecule, we limited the unit cell parameter metric to ±10% rather than ±20%. The application of this modified metric set 1 resulted in the retention of 166 structures. After M3 was applied, 2 viable candidate structures remained (denoted 6-617 and 2-452), both of which have R and Δ_{RMSD} values under the structural validation thresholds (Table 4; Fig. 2).

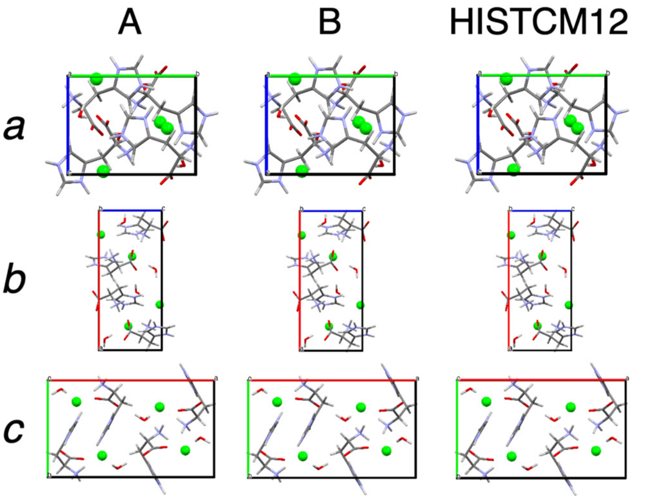

Fig. 2 A comparison of the geometry-optimized crystal structures of **Hist** determined by QNMRX-CSP along each of the crystallographic axes starting from the known crystal structure (A; §3.2) and an isolated molecule (B; §3.3), and the geometry-optimized crystal structure of **Hist** (HISTCM12).

3.3 QNMRX-CSP of zwitterionic organic HCl salts: starting from an isolated molecule

After benchmarking, we endeavored to use QNMRX-CSP for determining the crystal structures of **Orn** and **Hist** without reliance on their known crystal structures, in a manner that will be useful for future *de novo* structural predictions. Following the approaches of previous QNMRX-CSP studies,[40,41] we followed the steps of M1(B) to obtain a set of molecular fragments by subjecting structural models of the organic zwitterions centered in a 15 × 15 × 15 Å^3 unit cell of $P1$ space group symmetry to geometry optimizations. Although zwitterionic structural models were used as starting

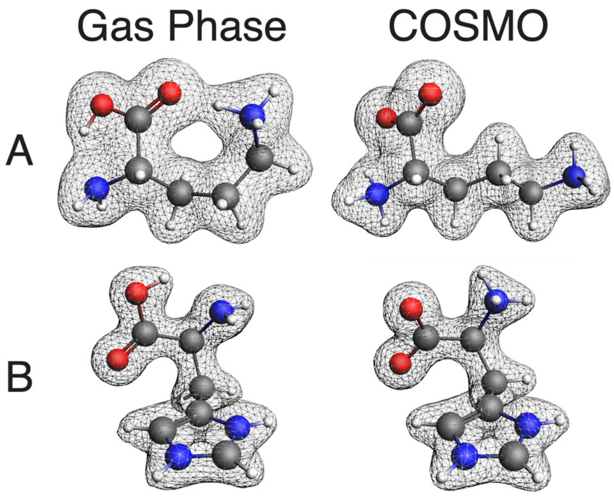

Fig. 3 Organic fragments and their electron density isosurfaces for (A) **Orn** and (B) **Hist** following either a gas phase geometry optimization in CASTEP (gas phase) or an ADF (COSMO) geometry optimization.

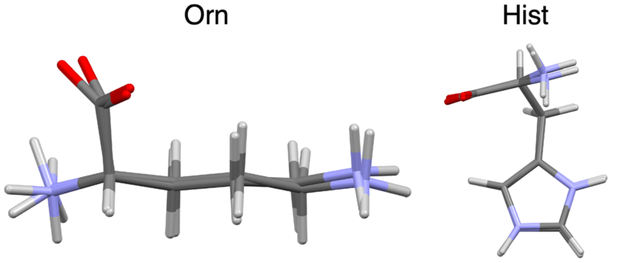

Fig. 4 Overlays of the refined zwitterionic organic fragments for **Orn** (left) and **Hist** (right), comparing the (i) ADF (COSMO) geometry-optimized organic molecular fragments and (ii) the corresponding organic fragments from the geometry-optimized structural models derived from the known crystal structures.

points, the geometry optimizations for both **Orn** and **Hist** converged to organic cationic forms (Fig. 3, left). To address this outcome, geometry optimizations were performed in ADF using the COSMO model (§2.2), which treats the solvent as a continuous polarizable medium that adjusts the electrostatic potential around the organic fragments to account for solvent-like stabilization of the charged functional groups. ADF (COSMO) calculations resulted in structural models representing organic zwitterionic cations (Fig. 3, right), which have distinct molecular conformations in comparison to the CASTEP-derived gas-phase models. In fact, the zwitterionic cations obtained from ADF (COSMO) optimizations are found to be similar to the zwitterionic cations from geometry-optimized ORNHCL12 and HISTCM12 structural models (§3.1, M1(A)), with comparative Δ_{RMSD} values of 0.313 Å and 0.149 Å, respectively (Fig. 4). The remainder of the steps in M1(B) were then applied to both **Orn** and **Hist**.

In the case of **Orn**, Polymorph generated 52 017 candidate structures, significantly exceeding the 30 733 candidate structures predicted by the protocol described in §3.2. Furthermore, after the application of metric set 1, 749 candidates were retained, which is an order of magnitude greater than those in §3.2 (Table 3). This difference in the number of candidate structures is due, in part, to the distinct molecular configurations and electronic structures of the ADF (COSMO) zwitterionic cation and the geometry-optimized ORNHCL12 (Fig. 4). Despite the increase in the number of candidate structures, after M3 was applied, 3 candidate structures were retained, each with R and Δ_{RMSD} values below the structural validation thresholds, thereby making them good matches to the geometry-optimized ORNHCL12 structure (Table 4; Fig. 1).

The application of Polymorph to the ADF (COSMO) zwitterionic cation of **Hist** resulted in 63 542 candidate structures, which is similar to the 64 952 candidate structures described for benchmarking calculations in §3.2. This demonstrates that the zwitterionic fragments in each scenario are similar enough that M2 results in similar packing. After applying metric set 1 and M3, 2 candidate structures were retained and validated as good structural matches by calculating the R and Δ_{RMSD} values (Table 4; Fig. 2).

4. Conclusions

QNMRX-CSP can generate structural models of zwitterionic organic HCl salts that are consistent with known crystal structures, whether initiated from a known crystal structure or molecular fragments derived solely from a 2D molecular diagram. We have found that the proposed gas-phase DFT-D2* geometry optimization in M1 used in previous QNMRX-CSP applications is inadequate for generating reasonable starting molecular fragments for zwitterions. In contrast, geometry optimizations using the COSMO water-solvation model yield realistic molecular fragments. However, the use of COSMO comes with certain pitfalls, as illustrated by the **Orn** example, where initiating the QNMRX-CSP protocol from a molecular fragment with a slightly inaccurate conformation led to a substantial increase in the number of candidate structures requiring evaluation. Future studies should seek to remedy this issue by incorporating more sophisticated molecular conformational screening approaches to identify all possible conformations of a flexible molecule. At the front end of QNMRX-CSP, a broader range of SSNMR data would be integrated, such as ^{1}H, ^{13}C, and ^{15}N chemical shifts, as well as ^{14}N and/or ^{17}O EFG tensors, to better identify plausible molecular conformations and protonation sites before using these models as starting points in CSP. Although this approach incurs an increased computational cost, QNMRX-CSP successfully identified a candidate structure for **Orn** that closely matches the known crystal structure. Lastly, QNMRX-CSP also determined, for the first time, a candidate structure for an organic HCl salt hydrate, **Hist**, showing promise for future investigations of solvated species. Finally, these results highlight the exciting prospect that QNMRX-CSP could enable the discovery of previously unobserved solid forms, including elusive polymorphs.

Author contributions

C. H. Fleischer III conducted QNMRX-CSP, calculated the NMR tensors, and performed statistical analysis. C. H. Fleischer III, S. T. Holmes, and R. W. Schurko contributed to project conceptualization, as well as writing and editing the manuscript.

Conflicts of interest

There are no conflicts to declare.

Data availability

The additional data sets supporting this article have been uploaded as part of the supplementary information (SI).

Supplementary information is available. See DOI: https://doi.org/10.1039/d5ce00899a.

Acknowledgements

R. W. S. is grateful for research support from The Florida State University and the National High Magnetic Field Laboratory (NHMFL), which is funded by the National Science Foundation Cooperative Agreement (DMR-2128556) and by the State of Florida. This work was supported in part by the U.S. Department of Energy, Office of Science, Office of Basic Energy Sciences, under Award Number DE-SC0022310, covering expenses related to postdoctoral salary.

References

1 R. K. Harris, NMR Crystallography: The Use of Chemical Shifts, *Solid State Sci.*, 2004, **6**(10), 1025–1037, DOI: 10.1016/j.solidstatesciences.2004.03.040.

2 R. E. Wasylishen, R. K. Harris and M. J. Duer, *NMR Crystallography*, A Wiley & Sons, New York, NY, 2009.

3 C. Martineau, J. Senker and F. Taulelle, NMR Crystallography, in *Annual Reports on NMR Spectroscopy*, 2014, vol. 82, pp. 1–57, DOI: 10.1016/B978-0-12-800184-4.00001-1.

4 S. E. Ashbrook and D. McKay, Combining Solid-State NMR Spectroscopy with First-Principles Calculations – a Guide to NMR Crystallography, *Chem. Commun.*, 2016, **52**(45), 7186–7204, DOI: 10.1039/C6CC02542K.

5 *Modern NMR Crystallography*, ed. D. L. Bryce, Royal Society of Chemistry, 2025, DOI: 10.1039/9781837673179.

6 B. Reif, S. E. Ashbrook, L. Emsley and M. Hong, Solid-State NMR Spectroscopy, *Nat. Rev. Methods Primers*, 2021, **1**, 1–23, DOI: 10.1038/s43586-020-00002-1.

7 A. A. Bunaciu, E. G. Udriştioiu and H. Y. Aboul-Enein, X-Ray Diffraction: Instrumentation and Applications, *Crit. Rev. Anal. Chem.*, 2015, **45**(4), 289–299, DOI: 10.1080/10408347.2014.949616.

8 E. S. Ameh, A Review of Basic Crystallography and X-Ray Diffraction Applications, *Int. J. Adv. Manuf. Tech.*, 2019, **105**(7–8), 3289–3302, DOI: 10.1007/s00170-019-04508-1.

9 R. L. C. Akkermans, N. A. Spenley and S. H. Robertson, Monte Carlo Methods in Materials Studio, *Mol. Simul.*, 2013, **39**(14–15), 1153–1164, DOI: 10.1080/08927022.2013.843775.

10 J. D. Gale, GULP: A Computer Program for the Symmetry-Adapted Simulation of Solids, *J. Chem. Soc., Faraday Trans.*, 1997, **93**(4), 629–637, DOI: 10.1039/a606455h.

11 C. W. Glass, A. R. Oganov and N. Hansen, USPEX—Evolutionary Crystal Structure Prediction, *Comput. Phys. Commun.*, 2006, **175**(11–12), 713–720, DOI: 10.1016/j.cpc.2006.07.020.

12 D. C. Lonie and E. Zurek, XtalOpt: An Open-Source Evolutionary Algorithm for Crystal Structure Prediction, *Comput. Phys. Commun.*, 2011, **182**(2), 372–387, DOI: 10.1016/j.cpc.2010.07.048.

13 C. J. Pickard and R. J. Needs, Ab Initio Random Structure Searching, *J. Phys.: Condens. Matter*, 2011, **23**(5), 053201, DOI: 10.1088/0953-8984/23/5/053201.

14 Y. Wang, J. Lv, L. Zhu and Y. Ma, CALYPSO: A Method for Crystal Structure Prediction, *Comput. Phys. Commun.*, 2012, **183**(10), 2063–2070, DOI: 10.1016/j.cpc.2012.05.008.

15 T. Yamashita, S. Kanehira, N. Sato, H. Kino, K. Terayama, H. Sawahata, T. Sato, F. Utsuno, K. Tsuda, T. Miyake and T. Oguchi, CrySPY: A Crystal Structure Prediction Tool Accelerated by Machine Learning, *Sci. Technol. Adv. Mater.: Methods*, 2021, **1**(1), 87–97, DOI: 10.1080/27660400.2021.1943171.

16 J. Wang, H. Gao, Y. Han, C. Ding, S. Pan, Y. Wang, Q. Jia, H.-T. Wang, D. Xing and J. Sun, MAGUS: Machine Learning and Graph Theory Assisted Universal Structure Searcher, *Natl. Sci. Rev.*, 2023, **10**(7), DOI: 10.1093/nsr/nwad128.

17 K. Wolinski, J. F. Hinton and P. Pulay, Efficient Implementation of the Gauge-Independent Atomic Orbital Method for NMR Chemical Shift Calculations, *J. Am. Chem. Soc.*, 1990, **112**(23), 8251–8260, DOI: 10.1021/ja00179a005.

18 C. J. Pickard and F. Mauri, All-Electron Magnetic Response with Pseudopotentials: NMR Chemical Shifts, *Phys. Rev. B: Condens. Matter Mater. Phys.*, 2001, **63**(24), 245101, DOI: 10.1103/PhysRevB.63.245101.

19 M. Cordova, E. A. Engel, A. Stefaniuk, F. Paruzzo, A. Hofstetter, M. Ceriotti and L. Emsley, A Machine Learning Model of Chemical Shifts for Chemically and Structurally Diverse Molecular Solids, *J. Phys. Chem. C*, 2022, **126**(39), 16710–16720, DOI: 10.1021/acs.jpcc.2c03854.

20 C. S. Vojvodin, S. T. Holmes, L. K. Watanabe, J. M. Rawson and R. W. Schurko, Multi-Component Crystals Containing Urea: Mechanochemical Synthesis and Characterization by 35Cl Solid-State NMR Spectroscopy and DFT Calculations, *CrystEngComm*, 2022, **24**(14), 2626–2641, DOI: 10.1039/D1CE01610E.

21 C. S. Vojvodin, J. E. Sanchez, S. T. Holmes, X. Lin and R. W. Schurko, Mechanochemical Synthesis and NMR Crystallography of Multicomponent Crystals: New Perspectives from Chlorine and Alkali Metal Solid-State NMR Spectroscopy, *Cryst. Growth Des.*, 2025, DOI: 10.1021/acs.cgd.5c00540.

22 R. K. Harris, P. Y. Ghi, R. B. Hammond, C. Y. Ma and K. J. Roberts, Refinement of Hydrogen Atomic Position in a Hydrogen Bond Using a Combination of Solid-State NMR and Computation, *Chem. Commun.*, 2003(22), 2834–2835, DOI: 10.1039/b309302f.

23 J. Cui, D. L. Olmsted, A. K. Mehta, M. Asta and S. E. Hayes, NMR Crystallography: Evaluation of Hydrogen Positions in Hydromagnesite by 13 C{ 1 H} REDOR Solid-State NMR and Density Functional Theory Calculation of Chemical Shielding Tensors, *Angew. Chem.*, 2019, **131**(13), 4254–4260, DOI: 10.1002/ange.201813306.

24 M. Cordova, P. Moutzouri, S. O. Nilsson Lill, A. Cousen, M. Kearns, S. T. Norberg, A. Svensk Ankarberg, J. McCabe, A. C. Pinon, S. Schantz and L. Emsley, Atomic-Level Structure Determination of Amorphous Molecular Solids by NMR, *Nat. Commun.*, 2023, **14**(1), 5138, DOI: 10.1038/s41467-023-40853-2.

25 J. B. Holmes, D. Torodii, M. Balodis, M. Cordova, A. Hofstetter, F. Paruzzo, S. O. Nilsson Lill, E. Eriksson, P.

Berruyer, B. Simões de Almeida, M. Quayle, S. Norberg, A. S. Ankarberg, S. Schantz and L. Emsley, Atomic-Level Structure of the Amorphous Drug Atuliflapon via NMR Crystallography, *Faraday Discuss.*, 2025, **255**, 342–354, DOI: 10.1039/D4FD00078A.

26 E. Salager, G. M. Day, R. S. Stein, C. J. Pickard, B. Elena and L. Emsley, Powder Crystallography by Combined Crystal Structure Prediction and High-Resolution1H Solid-State NMR Spectroscopy, *J. Am. Chem. Soc.*, 2010, **132**(8), 2564–2566, DOI: 10.1021/ja909449k.

27 M. Baias, J.-N. Dumez, P. H. Svensson, S. Schantz, G. M. Day and L. Emsley, De Novo Determination of the Crystal Structure of a Large Drug Molecule by Crystal Structure Prediction-Based Powder NMR Crystallography, *J. Am. Chem. Soc.*, 2013, **135**(46), 17501–17507, DOI: 10.1021/ja4088874.

28 C. M. Widdifield, S. O. Nilsson Lill, A. Broo, M. Lindkvist, A. Pettersen, A. Svensk Ankarberg, P. Aldred, S. Schantz and L. Emsley, Does Z ′ Equal 1 or 2? Enhanced Powder NMR Crystallography Verification of a Disordered Room Temperature Crystal Structure of a P38 Inhibitor for Chronic Obstructive Pulmonary Disease, *Phys. Chem. Chem. Phys.*, 2017, **19**(25), 16650–16661, DOI: 10.1039/c7cp02349a.

29 R. Toomey, L. Wang, E. C. Heider, J. D. Hartman, A. J. Nichols, D. A. A. Myles, A. S. Gardberg, G. J. McIntyre, M. Zeller, M. A. Mehta and J. K. Harper, NMR-Guided Refinement of Crystal Structures Using 15N Chemical Shift Tensors, *CrystEngComm*, 2024, **26**(25), 3289–3302, DOI: 10.1039/d4ce00237g.

30 M. R. Chierotti and R. Gobetto, NMR Crystallography: The Use of Dipolar Interactions in Polymorph and Co-Crystal Investigation, *CrystEngComm*, 2013, **15**(43), 8599–8612, DOI: 10.1039/c3ce41026a.

31 F. A. Perras, I. Korobkov and D. L. Bryce, NMR Crystallography of Sodium Diphosphates: Combining Dipolar, Shielding, Quadrupolar, Diffraction, and Computational Information, *CrystEngComm*, 2013, **15**(43), 8727–8738, DOI: 10.1039/c3ce40875b.

32 P. Thureau, S. Sturniolo, M. Zilka, F. Ziarelli, S. Viel, J. R. Yates and G. Mollica, Reducing the Computational Cost of NMR Crystallography of Organic Powders at Natural Isotopic Abundance with the Help of 13C-13C Dipolar Couplings, *Magn. Reson. Chem.*, 2019, **57**(5), 256–264, DOI: 10.1002/mrc.4848.

33 N. T. Duong, S. Raran-Kurussi, Y. Nishiyama and V. Agarwal, Quantitative 1H-1H Distances in Protonated Solids by Frequency-Selective Recoupling at Fast Magic Angle Spinning NMR, *J. Phys. Chem. Lett.*, 2018, **9**(20), 5948–5954, DOI: 10.1021/acs.jpclett.8b02189.

34 P. Raval, J. Trébosc, T. Pawlak, Y. Nishiyama, S. P. Brown and G. N. Manjunatha Reddy, Combining Heteronuclear Correlation NMR with Spin-Diffusion to Detect Relayed Cl–H–H and N–H–H Proximities in Molecular Solids, *Solid State Nucl. Magn. Reson.*, 2022, **120**, 0–11, DOI: 10.1016/j.ssnmr.2022.101808.

35 J. Dutour, N. Guillou, C. Huguenard, F. Taulelle, C. Mellot-Draznieks and G. Férey, Chiolite, a Case Study for Combining NMR Crystallography, Diffraction and Structural Simulation, *Solid State Sci.*, 2004, **6**(10), 1059–1067, DOI: 10.1016/j.solidstatesciences.2004.07.031.

36 H. J. Jakobsen, A. R. Hove, R. G. Hazell, H. Bildsøe and J. Skibsted, Solid-state 14N MAS NMR of Ammonium Ions as a Spy to Structural Insights for Ammonium Salts, *Magn. Reson. Chem.*, 2006, **44**(3), 348–356, DOI: 10.1002/mrc.1772.

37 H. Hamaed, J. M. Pawlowski, B. F. T. Cooper, R. Fu, S. H. Eichhorn and R. W. Schurko, Application of Solid-State ^{35} Cl NMR to the Structural Characterization of Hydrochloride Pharmaceuticals and Their Polymorphs, *J. Am. Chem. Soc.*, 2008, **130**(33), 11056–11065, DOI: 10.1021/ja802486q.

38 D. L. Bryce, Calcium Binding Environments Probed by 43Ca NMR Spectroscopy, *Dalton Trans.*, 2010, **39**(37), 8593, DOI: 10.1039/c0dt00416b.

39 F. A. Perras and D. L. Bryce, Multinuclear Magnetic Resonance Crystallographic Structure Refinement and Cross-Validation Using Experimental and Computed Electric Field Gradients: Application to Na2Al2B2O7, *J. Phys. Chem. C*, 2012, **116**(36), 19472–19482, DOI: 10.1021/jp308273h.

40 A. A. Peach, C. H. Fleischer, K. Levin, S. T. Holmes, J. E. Sanchez and R. W. Schurko, Quadrupolar NMR Crystallography Guided Crystal Structure Prediction (QNMRX-CSP), *CrystEngComm*, 2024, **26**(35), 4782–4803, DOI: 10.1039/D3CE01306E.

41 C. H. Fleischer, S. T. Holmes, K. Levin, S. L. Veinberg and R. W. Schurko, Characterization of Ephedrine HCl and Pseudoephedrine HCl Using Quadrupolar NMR Crystallography Guided Crystal Structure Prediction, *Faraday Discuss.*, 2025, **255**, 88–118, DOI: 10.1039/D4FD00089G.

42 F. M. Paruzzo, A. Hofstetter, F. Musil, S. De, M. Ceriotti and L. Emsley, Chemical Shifts in Molecular Solids by Machine Learning, *Nat. Commun.*, 2018, **9**(1), 4501, DOI: 10.1038/s41467-018-06972-x.

43 M. Kellner, J. B. Holmes, R. Rodriguez-Madrid, F. Viscosi, Y. Zhang, L. Emsley and M. Ceriotti, A Deep Learning Model for Chemical Shieldings in Molecular Organic Solids Including Anisotropy, *J. Phys. Chem. Lett.*, 2025, 8714–8722, DOI: 10.1021/acs.jpclett.5c01819.

44 S. P. Brown, Applications of High-Resolution 1H Solid-State NMR, *Solid State Nucl. Magn. Reson.*, 2012, 1–27, DOI: 10.1016/j.ssnmr.2011.11.006.

45 U. Sternberg, R. Witter, I. Kuprov, J. M. Lamley, A. Oss, J. R. Lewandowski and A. Samoson, 1H Line Width Dependence on MAS Speed in Solid State NMR – Comparison of Experiment and Simulation, *J. Magn. Reson.*, 2018, **291**, 32–39, DOI: 10.1016/j.jmr.2018.04.003.

46 M. Chávez, T. Wiegand, A. A. Malär, B. H. Meier and M. Ernst, Residual Dipolar Line Width in Magic-Angle Spinning Proton Solid-State NMR, *Magn. Reson.*, 2021, **2**(1), 499–509, DOI: 10.5194/mr-2-499-2021.

47 B. Simões de Almeida, D. Torodii, P. Moutzouri and L. Emsley, Barriers to Resolution in 1H NMR of Rotating Solids, *J. Magn. Reson.*, 2023, 355, DOI: 10.1016/j.jmr.2023.107557.

48 A. J. Vega, Quadrupolar Nuclei in Solids, in *Encyclopedia of Magnetic Resonance*, ed. D. M. Grant and R. K. Harris, John

Wiley & Sons, Ltd, Chichester, UK, 2007, pp. 3869–3888, DOI: 10.1002/9780470034590.emrstm0431.

49 J. Autschbach, S. Zheng and R. W. Schurko, Analysis of Electric Field Gradient Tensors at Quadrupolar Nuclei in Common Structural Motifs, *Concepts Magn. Reson., Part A*, 2010, **36**(2), 84–126, DOI: 10.1002/cmr.a.20155.

50 S. T. Holmes, C. S. Vojvodin and R. W. Schurko, Dispersion-Corrected DFT Methods for Applications in Nuclear Magnetic Resonance Crystallography, *J. Phys. Chem. A*, 2020, **124**(49), 10312–10323, DOI: 10.1021/acs.jpca.0c06372.

51 C. H. Fleischer, S. T. Holmes, X. Lin and R. W. Schurko, De Novo Crystal Structure Determination of L-Alaninamide HCl by Quadrupolar NMR Crystallography Guided Crystal Structure Prediction (QNMRX-CSP), *Solid State Nucl. Magn. Reson.*, 2025, **140**, 102034, DOI: 10.1016/j.ssnmr.2025.102034.

52 B. Dittrich, P. Munshi and M. A. Spackman, Redetermination, Invariom-Model and Multipole Refinement of L -Ornithine Hydrochloride, *Acta Crystallogr., Sect. B: Struct. Sci.*, 2007, **63**(3), 505–509, DOI: 10.1107/S0108768107014838.

53 H. Fuess, D. Hohlwein and S. A. Mason, Neutron Diffraction Study of L-Histidine Hydrochloride Monohydrate, *Acta Crystallogr., Sect. B: Struct. Sci.*, 1977, **33**(3), 654–659, DOI: 10.1107/S0567740877004415.

54 S. T. Holmes, J. M. Hook and R. W. Schurko, Nutraceuticals in Bulk and Dosage Forms: Analysis by 35Cl and 14N Solid-State NMR and DFT Calculations, *Mol. Pharmaceutics*, 2022, **19**(2), 440–455, DOI: 10.1021/acs.molpharmaceut.1c00708.

55 O. Socha, P. Hodgkinson, C. M. Widdifield, J. R. Yates and M. Dračínský, Exploring Systematic Discrepancies in DFT Calculations of Chlorine Nuclear Quadrupole Couplings, *J. Phys. Chem. A*, 2017, **121**(21), 4103–4113, DOI: 10.1021/acs.jpca.7b02810.

56 M. K. Pandey, H. Kato, Y. Ishii and Y. Nishiyama, Two-Dimensional Proton-Detected 35Cl/1H Correlation Solid-State NMR Experiment under Fast Magic Angle Sample Spinning: Application to Pharmaceutical Compounds, *Phys. Chem. Chem. Phys.*, 2016, **18**(8), 6209–6216, DOI: 10.1039/c5cp06042g.

57 D. A. Hirsh, A. J. Rossini, L. Emsley and R. W. Schurko, 35Cl Dynamic Nuclear Polarization Solid-State NMR of Active Pharmaceutical Ingredients, *Phys. Chem. Chem. Phys.*, 2016, **18**(37), 25893–25904, DOI: 10.1039/c6cp04353d.

58 G. te Velde, F. M. Bickelhaupt, E. J. Baerends, C. Fonseca Guerra, S. J. A. van Gisbergen, J. G. Snijders and T. Ziegler, Chemistry with ADF, *J. Comput. Chem.*, 2001, **22**(9), 931–967, DOI: 10.1002/jcc.1056.

59 S. J. Clark, M. D. Segall, C. J. Pickard, P. J. Hasnip, M. I. J. Probert, K. Refson and M. C. Payne, First Principles Methods Using CASTEP, *Z. Kristallogr.*, 2005, **220**(5–6), 567–570, DOI: 10.1524/zkri.220.5.567.65075.

60 A. Klamt and G. Schüürmann, COSMO: A New Approach to Dielectric Screening in Solvents with Explicit Expressions for the Screening Energy and Its Gradient, *J. Chem. Soc., Perkin Trans. 2*, 1993, **5**, 799–805, DOI: 10.1039/P29930000799.

61 C. C. Pye and T. Ziegler, An Implementation of the Conductor-like Screening Model of Solvation within the Amsterdam Density Functional Package, *Theor. Chem. Acc.*, 1999, **101**(6), 396–408, DOI: 10.1007/s002140050457.

62 N. L. Allinger, X. Zhou and J. Bergsma, Molecular Mechanics Parameters, *J. Mol. Struct.*, 1994, **312**(1), 69–83, DOI: 10.1016/S0166-1280(09)80008-0.

63 B. Hammer, L. B. Hansen and J. K. Nørskov, Improved Adsorption Energetics within Density-Functional Theory Using Revised Perdew-Burke-Ernzerhof Functionals, *Phys. Rev. B: Condens. Matter Mater. Phys.*, 1999, **59**(11), 7413–7421, DOI: 10.1103/PhysRevB.59.7413.

64 E. Van Lenthe and E. J. Baerends, Optimized Slater-Type Basis Sets for the Elements 1-118, *J. Comput. Chem.*, 2003, **24**(9), 1142–1156, DOI: 10.1002/jcc.10255.

65 E. S. Sachs, J. Hinze and N. H. Sabelli, Frozen Core Approximation, a Pseudopotential Method Tested on Six States of NaH, *J. Chem. Phys.*, 1975, **62**(9), 3393–3398, DOI: 10.1063/1.430993.

66 S. L. Mayo, B. D. Olafson and W. A. Goddard, DREIDING: A Generic Force Field for Molecular Simulations, *J. Phys. Chem.*, 1990, **94**(26), 8897–8909, DOI: 10.1021/j100389a010.

67 B. G. Pfrommer, M. Côté, S. G. Louie and M. L. Cohen, Relaxation of Crystals with the Quasi-Newton Method, *J. Comput. Phys.*, 1997, **131**(1), 233–240, DOI: 10.1006/jcph.1996.5612.

68 J. R. Yates, C. J. Pickard and F. Mauri, Calculation of NMR Chemical Shifts for Extended Systems Using Ultrasoft Pseudopotentials, *Phys. Rev. B: Condens. Matter Mater. Phys.*, 2007, **76**(2), 024401, DOI: 10.1103/PhysRevB.76.024401.

69 E. van Lenthe, J. G. Snijders and E. J. Baerends, The Zero-Order Regular Approximation for Relativistic Effects: The Effect of Spin–Orbit Coupling in Closed Shell Molecules, *J. Chem. Phys.*, 1996, **105**(15), 6505–6516, DOI: 10.1063/1.472460.

70 H. J. Monkhorst and J. D. Pack, Special Points for Brillouin-Zone Integrations, *Phys. Rev. B: Solid State*, 1976, **13**(12), 5188–5192, DOI: 10.1103/PhysRevB.13.5188.

71 P. Pyykkö, Year-2017 Nuclear Quadrupole Moments, *Mol. Phys.*, 2018, **116**(10), 1328–1338, DOI: 10.1080/00268976.2018.1426131.

72 D. W. Alderman, M. H. Sherwood and D. M. Grant, Comparing, Modeling, and Assigning Chemical-Shift Tensors in the Cartesian, Irreducible Spherical, and Icosahedral Representations, *J. Magn. Reson., Ser. A*, 1993, **101**(2), 188–197, DOI: 10.1006/jmra.1993.1029.

73 G. Barr, W. Dong, C. J. Gilmore, A. Kern, A. Parkin and C. C. Wilson, Using the Cambridge Structural Database to Validate Powder Structures, *Z. Kristallogr.*, 2007, **2007**(suppl_26), 209–214, DOI: 10.1524/zkri.2007.2007.suppl_26.209.

74 L. M. Hunnisett, N. Francia, J. Nyman, N. S. Abraham, S. Aitipamula, T. Alkhidir, M. Almehairbi, A. Anelli, D. M. Anstine, J. E. Anthony, J. E. Arnold and J. C. Cole, *et al.*, The Seventh Blind Test of Crystal Structure Prediction: Structure

Ranking Methods, *Acta Crystallogr., Sect. B: Struct. Sci., Cryst. Eng. Mater.*, 2024, **80**(6), 548–574, DOI: 10.1107/S2052520624008679.

75 L. M. Hunnisett, J. Nyman, N. Francia, N. S. Abraham, C. S. Adjiman, S. Aitipamula, T. Alkhidir, M. Almehairbi, A. Anelli, D. M. Anstine, J. E. Anthony and J. C. Cole, *et al.*, The Seventh Blind Test of Crystal Structure Prediction: Structure Generation Methods, *Acta Crystallogr., Sect. B:Struct. Sci., Cryst. Eng. Mater.*, 2024, **80**(6), 517–547, DOI: 10.1107/S2052520624007492.